The Astronomical Journal, 133:1393–1408, 2007 April

DENSITIES OF SOLAR SYSTEM OBJECTS FROM THEIR ROTATIONAL LIGHT CURVES

Pedro Lacerda[1] and David C. Jewitt
Institute for Astronomy, University of Hawaii, Honolulu, HI, USA
Received 2006 October 6; accepted 2006 December 1

ABSTRACT

We present models of the shapes of four Kuiper Belt objects (KBOs) and the Jovian Trojan asteroid (624) Hektor as ellipsoidal figures of equilibrium and Roche binaries. Our simulations select those figures of equilibrium whose light curves best match the measured rotational data. The best-fit shapes, combined with the knowledge of the spin period of the objects, provide estimates of the bulk densities of these objects. We find that the light curves of KBOs (20000) Varuna and 2003 EL_{61} are well matched by Jacobi triaxial ellipsoid models with bulk densities 992^{+86}_{-15} and 2551^{+115}_{-10} kg m^{-3}, respectively. The light curves of (624) Hektor and KBO 2001 QG_{298} are well described by Roche contact-binary models with densities 2480^{+292}_{-80} and 590^{+143}_{-47} kg m^{-3}, respectively. The nature of 2000 GN_{171} remains unclear: Roche binary and Jacobi ellipsoid fits to this KBO are equivalent but predict different densities, $\sim$2000 and $\sim$650 kg m^{-3}, respectively. Our density estimates suggest a trend of increasing density with size.

Key words: Kuiper Belt — minor planets, asteroids — solar system: general

1. INTRODUCTION

Most small bodies of the solar system appear unresolved at the $\sim$0.05″ peak angular resolution offered by current technology. As a consequence, information about the shapes and rotations of the small bodies must be inferred, principally from measurements of the time dependence of the scattered radiation. So-called light-curve inversion techniques have been used for decades to study the rotational properties of main-belt asteroids (Cellino et al. 1989; Kaasalainen et al. 2002). At their simplest, these involve using the peak-to-peak interval of the light curve to estimate the rotation period and the peak-to-peak brightness variation to estimate the axis ratio of bodies that are assumed to be triaxial in shape and in principal-axis rotation about the minor axis. At their most complex, the inversion techniques can be used to solve for the full three-dimensional shapes and rotation vectors, using observations from a range of aspect angles (Kaasalainen & Torppa 2001; Kaasalainen et al. 2001).

All light-curve interpretations are subject to an ambiguity between variations caused by shape and variations caused by non-uniform surface albedo, as clearly expressed a century ago by Russell (1906). This ambiguity can be broken when simultaneous optical and thermal observations are available, as is the case for some of the larger asteroids in the main belt. Numerous observations of this type have shown that, with rare exceptions, the albedos of the asteroids do not vary over their surfaces by a large amount (Degewij et al. 1979). This spatial uniformity could simply mean that the compositions are intrinsically uniform. Alternatively, real surface compositional variations could exist but be smoothed out by efficient lateral transport of dust over the surfaces of small bodies. The most famous exception to this rule is provided by Saturn's satellite Iapetus, which has a light-curve range of nearly 2 mag caused by surface albedo markings (Millis 1977). This case is pathological, however, in the sense that it appears to be a result of Iapetus' synchronous rotation about Saturn, which leads to unequal radiation and micrometeorite bombardment fluxes on the leading and trailing hemispheres of the satellite. This special geometric circumstance is presumably not relevant to the case of small bodies in heliocentric orbit.

In the outer solar system, lower temperatures and greater distances make the detection of thermal radiation increasingly challenging, even with the most sensitive infrared satellites in space (e.g., Cruikshank 2005). Consequently, only the reflected light curve is available, and the interpretation must be based on the assumption that the surface albedo variation is minimal. As we describe below, support for this assumption comes not only from the analogy with the (generally uniform) main-belt asteroids, but from the remarkably symmetric light curves displayed by most outer solar system objects. Rotational symmetry is expected for figures of equilibrium having uniform surface albedos but is not a natural consequence of surface albedo markings.

The light curves of several large Kuiper Belt objects (KBOs), notably (20000) Varuna (Jewitt & Sheppard 2002) and 2003 EL_{61} (Rabinowitz et al. 2006), suggest that these are high angular momentum bodies in which the shape has been deformed by rapid rotation. Other objects may be contact binary systems, as has long been suggested for Jovian Trojan asteroid (624) Hektor (Hartmann & Cruikshank 1978, 1980; Weidenschilling 1980) and, recently, for KBO 2001 QG_{298} (Sheppard & Jewitt 2004; Takahashi & Ip 2004). These systems are interesting since, under conditions of rotational equilibrium, the period and the shape (both of which can be inferred from light-curve data) are uniquely related to the bulk density. Light curves of these objects may thus be interpreted in terms of a fundamental geophysical property that is otherwise difficult to measure.

In this paper, we discuss the light curves of specific solar system bodies in terms of rotational equilibrium models, paying particular attention to high angular momentum systems and contact binaries. Our models address the effects of the surface scattering on the derived system parameters. Prototype contact binary (624) Hektor is examined in detail, taking advantage of voluminous high-quality data published for this object over a range of aspect angles (see Table 1). The models are then applied to four well-observed KBOs (Table 2) and used to place quantitative constraints on their properties in a consistent formalism. Indeed, the uniformity of approach is one of the strengths of our simulations.

2. LIGHT-CURVE SIMULATIONS

2.1. *Jacobi Ellipsoids*

The formalism associated with the ellipsoidal figures of equilibrium is described in great detail in Chandrasekhar (1969). A

[1] Also at GAUC, Departamento de Matemática, Universidade de Coimbra, Coimbra, Portugal.

TABLE 1

(624) Hektor Light-Curve Data

JD[a]	θ[b] (deg)	α[c] (deg)	$\Delta m_{\rm data}$[d] (mag)	$\Delta m_{\rm model}$[e] (mag)
2,435,989	74.9	+4.4	0.775	0.737
2,438,795	24.8	+4.1	0.113	0.063
2,439,556	52.5	−5.3	0.398	0.302
2,439,977	86.3	+4.1	1.055	1.048

Note.—Sources cited in § 3.1.
[a] Date of observation.
[b] Aspect angle.
[c] Phase angle.
[d] Data light-curve range.
[e] Best-fit model light-curve range.

homogeneous, fluid body spinning in free space will assume a shape that balances self-gravity and the inertial acceleration due to rotation. This means that the triaxial shape of such a body is a function of its spin frequency and density. The equilibrium figures of isolated, rotating bodies are the Maclaurin spheroids and the Jacobi ellipsoids. The former are oblate spheroids and the latter are triaxial ellipsoids, and in both cases the rotation is about the shortest physical axis. We are interested only in the Jacobi ellipsoids because oblate spheroids have rotational symmetry and thus produce flat light curves.

The shapes of Jacobi ellipsoids in terms of the semiaxes (a, b, c) can be obtained by solving (Chandrasekhar 1969)

$$a^2b^2\int_0^\infty \frac{1}{(a^2+u)(b^2+u)\Delta(a,b,c)}du = c^2\int_0^\infty \frac{1}{(c^2+u)\Delta(a,b,c)}du, \qquad (1)$$

where $\Delta(a,b,c) = \left[(a^2+u)(b^2+u)(c^2+u)\right]^{1/2}$. The spin frequency ω and density ρ are related to the shape by

$$\frac{\omega^2}{\pi G\rho} = 2abc\int_0^\infty \frac{u}{(a^2+u)(b^2+u)}du, \qquad (2)$$

where G is the gravitational constant. We solved equation (1) for values of b/a between 0.43 and 1.00 in steps of 0.01 and used the solutions, together with equation (2), to calculate $\omega^2/\pi G\rho$, which relates the spin period to the body density for each of the equilibrium triaxial ellipsoids. Figures with $b/a < 0.43$ are unstable due to rotational fission (Jeans 1919).

The derived shapes are then ray-traced at regular intervals spanning a full rotation period. This produces a set of frames from which the light curve is extracted by integrating the total light in each one of them. In this way we generate a database of light curves of figures of equilibrium that can be used to compare to the light-curve data. As described below we run our simulations for two surface-scattering laws.

The ray-tracing is done using the main engine of the open-source software POV-Ray.[2] The surface-scattering routines were rewritten to permit accurate control of the scattering function. To test the accuracy of our ray-tracing method we simulated the light curve of a triaxial ellipsoid with an axis ratio b/a, observed equator-on ($\theta = 0°$) at zero phase angle ($\alpha = 0°$), using a "lunar" surface-scattering function (see § 2.3), and compared the result with the analytical solution for the same configuration, given by

$$m(b/a, \phi) = 2.5\log_{10} \times \sqrt{1+\left[(b/a)^2-1\right]\cos^2(2\pi\phi)}, \qquad (3)$$

where $\phi \in [0, 1]$ is the rotational phase of the ellipsoid. The result is plotted in Figure 1. The ray-traced light curve deviates ~0.1% from the analytical solution, which is negligible when compared to the uncertainties in the photometric data, typically ~2–3% on real astronomical objects.

2.2. *Roche Binaries*

Light curves from an eclipsing binary asteroid consisting of two spheres in circular orbit have been presented by Wijesinghe & Tedesco (1979). As the binary separation becomes comparable to the scale of either component, mutual gravitational forces will deform the bodies, increasing the light-curve range over the maximum (factor of 2) possible for equal-sized spheres (Leone et al.

[2] Available at http://www.povray.org.

TABLE 2

List of Objects to Fit

Object[a]	Family[b]	H[c] (mag)	D_e[d] (km)	P[e] (hr)	Δm[f] (mag)	ρ[g] (kg m^{-3})
			Triaxial Ellipsoids			
2003 EL$_{61}$	KBO	0.2	1450	3.9154	0.28 ± 0.04	2585^{+81}_{-44}
Varuna	KBO	3.2	900	6.3442	0.42 ± 0.02	992^{+86}_{-15}
2000 GN$_{171}$	KBO	6.0	360	8.329	0.61 ± 0.03	1946^{+1380}_{-344}
			Roche Binaries			
2001 QG$_{298}$	KBO	6.9	240	13.7744	1.14 ± 0.04	590^{+143}_{-47}
2000 GN$_{171}$	KBO	6.0	360	8.329	0.61 ± 0.03	650^{+75}_{-80}
(624) Hektor	Trojan	7.5	180	6.9225	1.2[h]	2480^{+80}_{-292}

Note.—Sources cited in the text. KBO 2000 GN$_{171}$ is intentionally listed twice, as its nature is uncertain.
[a] Object designation.
[b] Object family.
[c] Absolute magnitude.
[d] Approximate equivalent circular diameter.
[e] Rotation period.
[f] Peak-to-peak light-curve range.
[g] Estimated density.
[h] Maximum predicted amplitude at $\theta = 90°$.

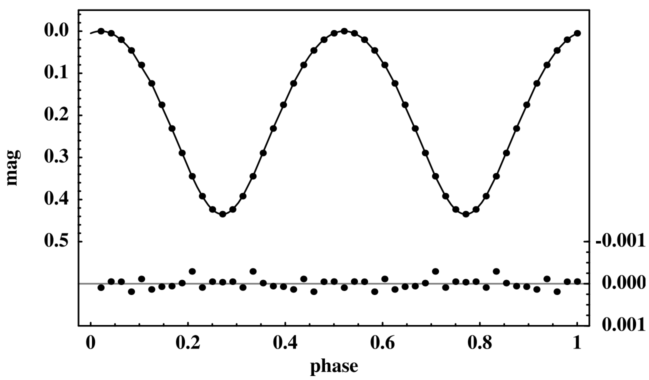

FIG. 1.—Accuracy of ray-traced vs. analytical solutions for an ellipsoid with a lunar-type surface and an axis ratio $b/a = 2/3$, observed at aspect angle $\theta = 90°$ and phase angle $\alpha = 0°$. Bottom dots and right ordinate axis show difference between the dots (ray-traced) and the line (analytical) shown at the top.

1984). To model this mutual deformation in close and contact-binary systems we use the Roche binary approximation (Chandrasekhar 1963; Leone et al. 1984). In this approximation each component is considered to be a Roche ellipsoid, which is the equilibrium shape of a satellite orbiting a spherical, more massive primary. The tidally deformed shape of the secondary is assumed to be solely caused by the spherically symmetric gravitational gradient due to the primary. Each component's shape is calculated separately using reciprocal values, q and $1/q$, for the mass ratio. Clearly, such an approximation introduces the most error when calculating shapes of close binaries with mass ratios near $q = 1$. In these situations the elongation of the binary components is underestimated, which leads to smaller light-curve ranges. With the further assumptions that the binary is tidally locked and that the components have equal density, ρ, and orbit the center mass in circular paths, the mass ratio q, the shape of one of the components (b/a, c/a), and the orbital frequency ω can be calculated by solving (Chandrasekhar 1963)

$$\frac{(3+1/q)a^2+c^2}{(1/q)b^2+c^2} = \frac{a^2A_1 - c^2A_3}{b^2A_2 - c^2A_3}, \tag{4a}$$

$$\frac{q}{1+q}\frac{\omega^2}{\pi G\rho} = 2abc\frac{a^2A_1 - c^2A_3}{(3+1/q)a^2+c^2}, \tag{4b}$$

with A_1, A_2, and A_3 given by (Chandrasekhar & Lebovitz 1962)

$$A_1 = \frac{2}{a^3\sin^3\phi}\frac{1}{\sin^2\theta}[F(\theta,\phi) - E(\theta,\phi)], \tag{5a}$$

$$A_2 = \frac{2}{a^3\sin^3\phi}\frac{1}{\sin^2\theta\cos^2\theta} \times \left[E(\theta,\phi) - F(\theta,\phi)\cos^2\theta - \left(\frac{c}{b}\right)\sin^2\theta\sin\phi\right], \tag{5b}$$

$$A_3 = \frac{2}{a^3\sin^3\phi}\frac{1}{\cos^2\theta}\left[\left(\frac{b}{c}\right)\sin\phi - E(\theta,\phi)\right], \tag{5c}$$

where $E(\theta,\phi)$ and $F(\theta,\phi)$ are the standard elliptic integrals of the two kinds with arguments

$$\theta = \arcsin\sqrt{\frac{a^2-b^2}{a^2-c^2}}, \quad \phi = \arccos\left(\frac{c}{a}\right). \tag{6}$$

Each root of equation (4a), corresponding to a Roche ellipsoid solution, can be calculated by setting three of the four parameters q and (a, b, c), and solving for the fourth by interpolation. For the primary, we set $a = 1$ and calculate b for each combination of $q = q_{\min}, \ldots, 1.00$ and $c = c_{\min}, \ldots, 0.99$, both in steps of 0.01. The procedure is repeated using $1/q$ instead of q to calculate the shape of the secondary, (a', b', c'). A valid Roche binary solution is obtained if two sets, (q, a, b, c) and $(1/q, a', b', c')$, yield the same value $\omega^2(\pi G\rho)^{-1}$ when replaced into the right-hand side of equation (4b). Table 3 shows the solutions for $q = 0.25$.

2.3. *Surface Scattering*

The surface-scattering properties of KBOs are unknown. For this reason the amount of sunlight reflected from a KBO is usually taken to be proportional to its geometrical cross-section. However, the total range of the light curve of a convex object increases significantly if there is limb darkening. The two simplest scattering laws generally used to model planetary surfaces are the Lommel-Seeliger and Lambert laws. The Lommel-Seeliger law is a single-scattering model, suitable for low-albedo surfaces, and can be considered a simplification of the well-known Hapke model (Li 2005). The Hapke model is inappropriate for this work because it

TABLE 3
ROCHE BINARY SOLUTIONS FOR MASS RATIO $q = 0.25$

B/A[a]	C/A[a]	b/a[b]	c/a[b]	$\omega^2/(\pi G\rho)$[c]	l[d]
0.91674	0.83000	0.51426	0.48000	0.10626	1.19222
0.92292	0.84000	0.61175	0.57000	0.10137	1.28193
0.92891	0.85000	0.66433	0.62000	0.09554	1.34473
0.93473	0.86000	0.70532	0.66000	0.08945	1.40392
0.94037	0.87000	0.73534	0.69000	0.08368	1.45810
0.94584	0.88000	0.76469	0.72000	0.07755	1.51789
0.95114	0.89000	0.79333	0.75000	0.07109	1.58466
0.95629	0.90000	0.81200	0.77000	0.06558	1.64436
0.96128	0.91000	0.83935	0.80000	0.05864	1.72902
0.96612	0.92000	0.85713	0.82000	0.05282	1.80713
0.97081	0.93000	0.88311	0.85000	0.04550	1.92216
0.97537	0.94000	0.89996	0.87000	0.03943	2.03365
0.97979	0.95000	0.91642	0.89000	0.03328	2.17018
0.98407	0.96000	0.93250	0.91000	0.02706	2.34450
0.98824	0.97000	0.95588	0.94000	0.01924	2.65422

[a] Primary axis ratios.
[b] Secondary axis ratios.
[c] Orbital frequency squared in units of $\pi G\rho$, where G is the gravitational constant.
[d] Orbital distance in units of $A + a$.

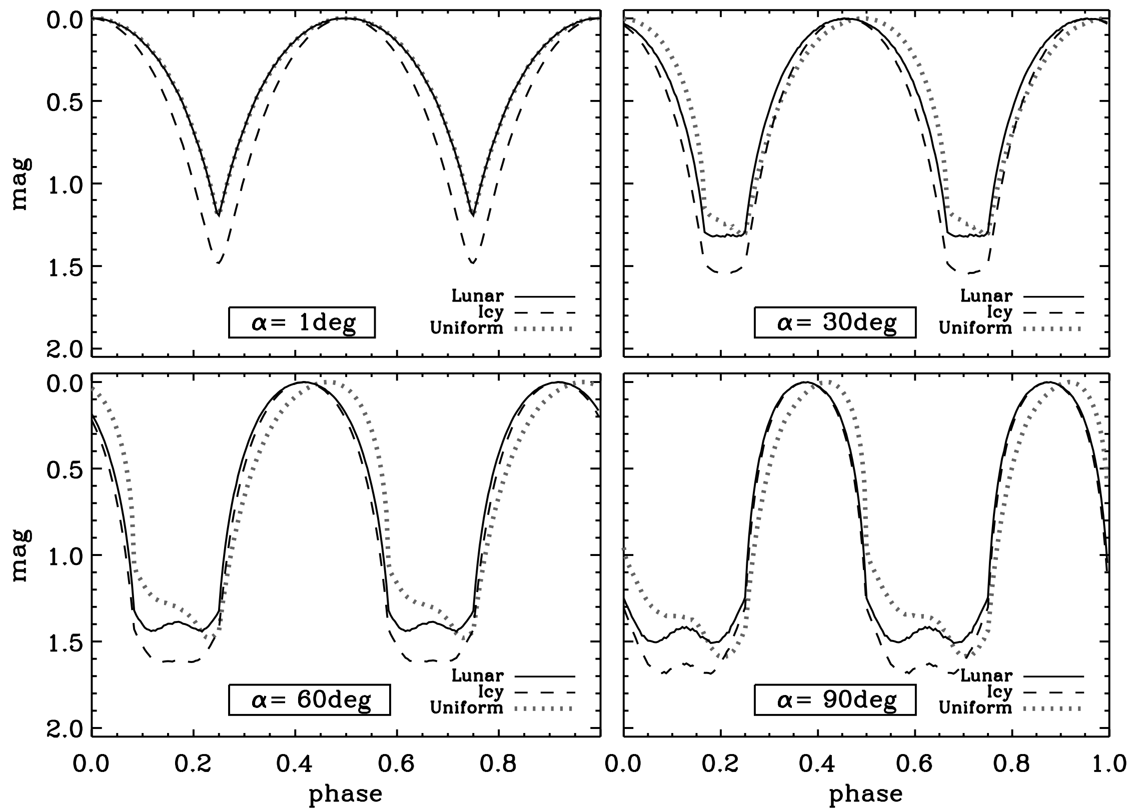

FIG. 2.—Light curves of a Roche contact binary at different phase angles and for different scattering laws. In the uniform case every point of the surface that is illuminated by sunlight reflects exactly the same amount of light back to the observer. Both primary and secondary have axis ratios $b/a = 0.67$ and $c/a = 0.60$, and the components are in contact.

has many parameters that cannot realistically be constrained using light-curve data. To model relative brightness variations, which is what is needed to generate light curves, the Lommel-Seeliger law requires no parameters; it depends solely on the cosines of the incidence and emission angles (i and e, the angles between the surface normal and the directions to the light source and to the observer). The Lommel-Seeliger reflectance function is thus

$$r_{\mathrm{LS}} \propto \frac{\mu_0}{\mu + \mu_0}, \tag{7}$$

where $\mu_0 = \cos i$ and $\mu = \cos e$.

The Lambert scattering law is a simple description of a perfectly diffuse surface. It assumes that a light ray that enters the material is multiply scattered and thus leaves the surface in a random direction. As such, it is a multiple-scattering law that adequately describes high-albedo surfaces. The Lambert reflectance function is

$$r_{\mathrm{L}} \propto \mu_0. \tag{8}$$

The Lommel-Seeliger and Lambert scattering functions are taken here as representative of low-albedo "lunar-type" surfaces and high-albedo "icy-type" surfaces, respectively.

Figures 2 and 3 compare the light curves of Roche contact binaries using both lunar and icy scattering models at four different phase angles. A uniform scattering law is also plotted for comparison. The uniform model assigns equal brightness to any illuminated point on the surface and thus represents the illuminated cross-section. Figure 2 is for a contact binary with equal size components, while Figure 3 represents the case of different sizes for primary and secondary (see Fig. 4). A few conclusions can immediately be drawn from inspection of Figures 2 and 3:

1. At low phase angle the lunar model produces negligible limb darkening and is thus equivalent to the simpler uniform model. Only at large phase angles ($\gtrsim 30°$) does the uniform approximation fail to follow the lunar scattering law. Icy surfaces, however, always produce larger light-curve ranges for the same shape, which implies that assuming uniform scattering when interpreting light curves of icy objects will tend to exaggerate the inferred shape elongation.
2. The light curve minima become broader with increasing phase angle. This fact implies that V-shaped minima are strictly diagnostic of a close-binary configuration only when viewed near zero phase angle. Fortunately, this is necessarily the case for all observations of KBOs.
3. Observations at different phase angles shift the minima and maxima of the light curve in rotational phase. This effect should be taken into account when fitting a single spin period to observations taken at different phase angles. For instance, failure to fit all the data with a single period does not necessarily imply complex (nonprincipal axis) rotation when observations over a wide range of phase angles are compared.

In our simulations we use the lunar- and icy-type surface laws separately to assess how different surface properties affect our results. As shown below, we find that different surface properties do not significantly change our density estimates. It is also shown that while in some cases the choice of a particular scattering law clearly improves the light-curve fit, in other cases the result is degenerate as far as surface properties are concerned. The simulations

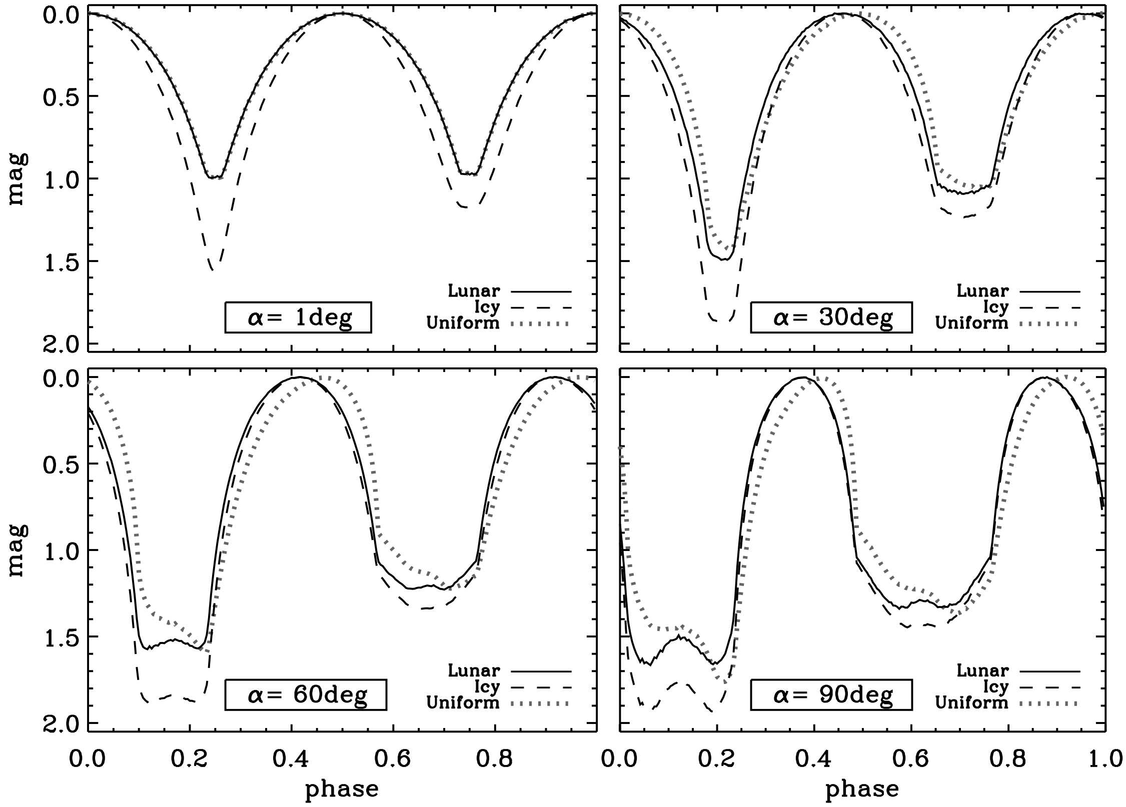

FIG. 3.—Same as Fig. 2, but for a binary with different size components. Mass ratio is $q = 0.67$, and the components have axis ratios ($B/A = 0.77$, $C/A = 0.69$) and ($b/a = 0.53$, $c/a = 0.49$).

further assume that the surface albedo is uniform and the same for both components of the binary.

2.4. *Observational Geometry*

Owing to their large distances from the Sun and Earth, KBOs can only be observed at small phase angles ($\alpha < 2°$). The object (20000) Varuna is known to exhibit a pronounced opposition effect at phase angle $\alpha < 0.1°$ (Hicks et al. 2005), which seems to affect the extent of its brightness variation (Belskaya et al. 2006). In the range $0.1° < \alpha < 2.0°$ the phase curve of (20000) Varuna is linear (Sheppard & Jewitt 2002) and the light curve unaffected by phase effects. We place our simulations well within this linear regime by using a phase angle $\alpha = 1°$. In addition, since most of the data being modeled have $\alpha > 0.1°$ the opposition effect is likely unimportant to the conclusions presented here.

The aspect angle is the angle between the line of sight and the spin axis of the system. We simulated light curves for two values of the aspect angle: 90° (equator-on) and 75°. Given that the spin axis orientations are unknown, the models with a tilted orientation allow us to investigate how the aspect angle affects our conclusions. In the case of (624) Hektor the spin (or orbital) axis orientation is known (Dunlap & Gehrels 1969), and we were able to perform simulations using the actual aspect and phase angles at the moment the data were taken (see Table 1).

3. BEST-FIT SOLUTIONS

3.1. *(624) Hektor*

Jovian Trojan asteroid (624) Hektor has long been recognized as a likely contact binary (Hartmann & Cruikshank 1978, 1980;

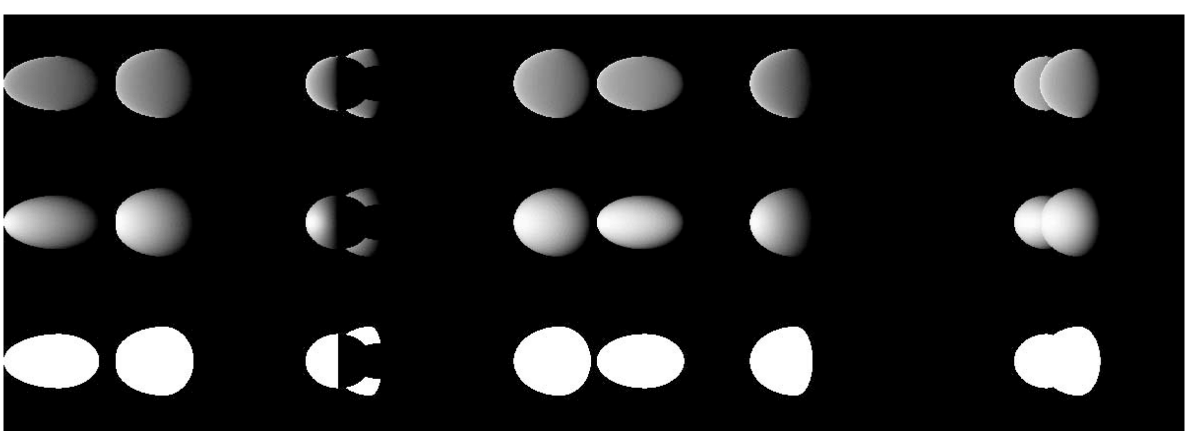

FIG. 4.—Three-dimensional rendering of the binary used to produce Fig. 3 ($\alpha = 60°$). Rotational phase ($\phi = 0°, 72°, 144°, 216°$, and 288°) runs from left to right, and rows show (*top to bottom*) lunar, icy, and uniform surface-scattering functions.

TABLE 4

Best Three Roche Binary Model Fits to (624) Hektor

ST[a]	q[b]	B/A[c]	C/A[c]	b/a[d]	c/a[d]	$\omega^2/(\pi G\rho)$[e]	$d/(A+a)$[f]	ρ[g]	$\chi^2/\chi^2_{\rm best}$[h]
Lunar	0.62	0.80	0.72	0.47	0.43	0.122	0.98	2480	1.00
Lunar	0.67	0.77	0.69	0.53	0.49	0.128	1.00	2374	1.06
Lunar	0.65	0.79	0.71	0.47	0.43	0.124	0.97	2453	1.08

[a] Surface type.
[b] Mass ratio of the binary components.
[c] Axis ratios of the primary.
[d] Axis ratios of the secondary.
[e] Orbital frequency of binary.
[f] Binary orbital separation.
[g] Bulk density of the bodies (in kg m^{-3}).
[h] Ratio of χ^2 of model to χ^2 of best-fit model.

Weidenschilling 1980). Numerous light-curve data spanning a long time base (1957–1968) have been collected for this object, which allowed the determination of the pole orientation (Dunlap & Gehrels 1969; de Angelis 1995). Depending on the orbital configuration, the light-curve range of (624) Hektor varies between 0.1 and 1.2 mag (see Table 1). As noted by Weidenschilling (1980; see also Leone et al. 1984) light-curve ranges above 0.9 mag cannot be produced by rotation of a single equilibrium figure and, instead, are most likely produced by a tidally distorted contact binary. Besides the large range of variability, the light-curve morphology of (624) Hektor exhibits V-shaped minima and round maxima, also characteristic of tidally deformed, contact binary systems.

Making use of the extensive data set presented in Dunlap & Gehrels (1969) we have selected the Roche binary model (see § 2.2) that simultaneously best fits the observations at four observing campaigns (see Table 1). The quality of fit is measured by $\chi^2/\chi^2_{\rm best}$, i.e., the ratio of the χ^2 value of each model to the χ^2 value of the best-fit model. This corresponds to a reduced χ^2 ($\chi^2_{\rm red}$) if one assumes that the best-fit model has $\chi^2_{\rm red} = 1$. We do this because the errors associated with the data for (624) Hektor are not known with certainty, which does not allow us to reliably calculate the $\chi^2_{\rm red}$ for each model. In Table 4 we show the three Roche models that best approximate (624) Hektor's light curve. Figure 5 shows how well our simulations are able to determine the density, orbital distance, mass ratio, and surface scattering properties of the (624) Hektor system. In the top left panel we plot histograms of quality of fit for the two scattering laws considered. A lunar scattering law clearly produces better fits, which is no surprise as (624) Hektor is known to have a low albedo

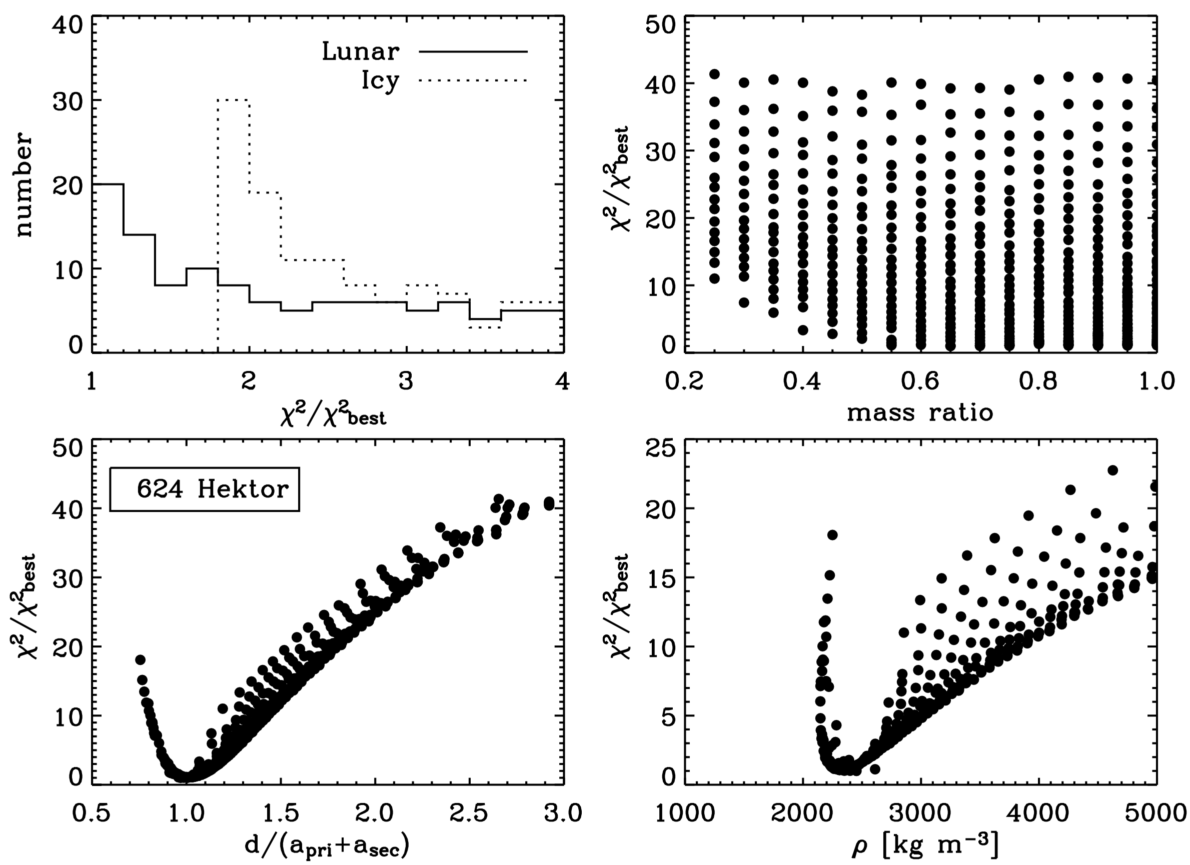

Fig. 5.—Quality of fit as a function of scattering function (*top left*), mass ratio of binary components (*top right*), orbital distance (*bottom left*), and bulk density of binary components (*bottom right*) for (624) Hektor. To avoid cluttering, only Roche models with mass ratio values, q, in multiples of 0.05 are plotted.

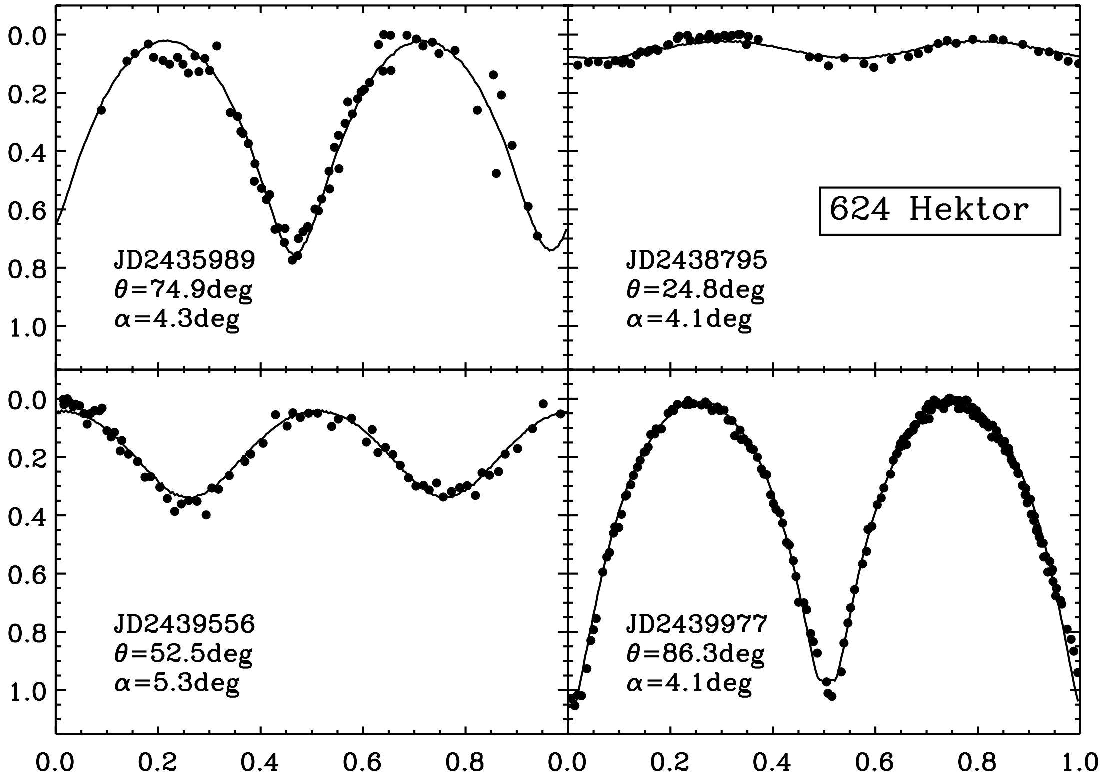

Fig. 6.—Roche binary model light curve superimposed on data for (624) Hektor taken at four different aspects.

(~0.06; Cruikshank 1977; Fernández et al. 2003). In the bottom left panel the orbital distance of the Roche binary models is plotted versus quality of fit. The orbital distance is given in units of the sum of the semimajor axes of the primary, A, and of the secondary, a. The minimum is centered around $d/(A + a) = 1$, which corresponds to the binary components being in contact. Values $d/(A + a) < 1$ are unphysical but we have decided to keep them for two reasons. First, they may result from the approximations of the Roche model (Leone et al. 1984). The orbital distance is calculated using Kepler's third law assuming point masses for the binary components. Since these have elongated shapes, gravity will be enhanced, meaning the Roche model may underestimate the orbital distance. Second, the mechanism that brought the two components together and formed the binary may have produced some deformation (a "crush" zone) around the point of contact, bringing the objects closer together than the situation of contact between two perfectly hard ellipsoids. Considering models with $\chi^2/\chi^2_{\rm best} < 2$, which roughly corresponds to a 1 σ criterion, we find that the two components of (624) Hektor are separated by $d/(A + a) = 1.00^{+0.11}_{-0.09}$, which is consistent with contact. Figure 5 (*top right*) shows that the model poorly constrains the mass ratio of the binary. The mass ratio that corresponds to the best-fit Roche binary is $q = 0.62$, but the range of q values that fall within 1 σ of the best fit is broad. As for the bulk density of (624)

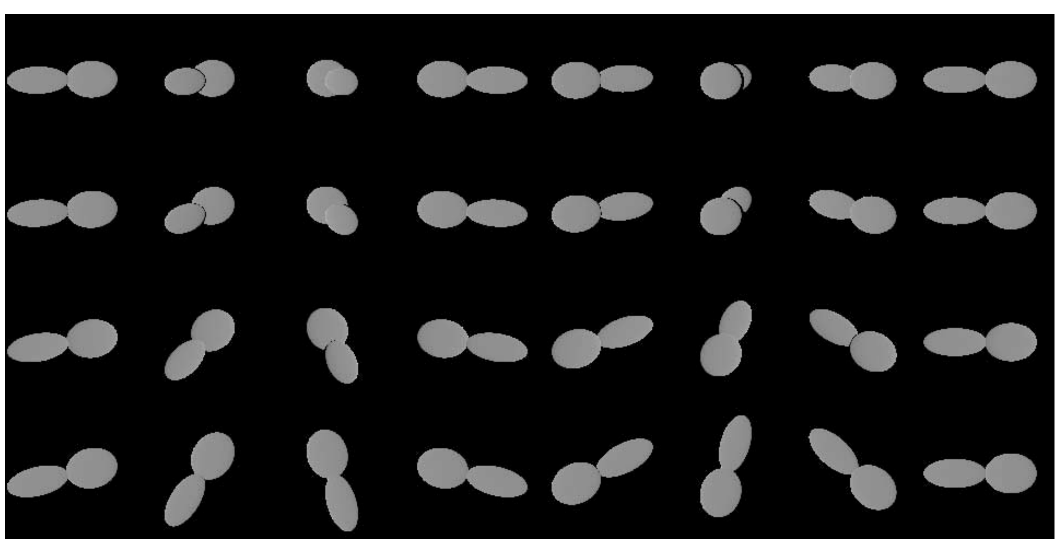

Fig. 7.—Rendering of best-fit Roche binary model for (624) Hektor for the four geometries listed in Table 1. Rotational phase ($\phi = 15°$, $60°$, $105°$, $165°$, $210°$, $255°$, $315°$, and $360°$) runs from left to right, while aspect angle decreases from top to bottom.

TABLE 5

2001 QG_{298} Model Fit

ST[a]	θ[b]	q[c]	B/A[d]	C/A[d]	b/a[e]	c/a[e]	$\omega^2/(\pi G\rho)$[f]	$d/(A+a)$[g]	ρ[h]	$\chi^2/\chi^2_{\rm best}$[i]
Jacobi Ellipsoid										
Lunar	90	...	0.43	0.34	...	...	0.283	...	271	2.21
Icy	90	...	0.56	0.41	...	...	0.327	...	234	2.50
Lunar	75	...	0.43	0.34	...	...	0.283	...	271	6.60
Icy	75	...	0.50	0.38	...	...	0.310	...	248	2.51
Roche Binary										
Lunar	90	0.84	0.72	0.65	0.45	0.41	0.130	0.90	590	1.00
Icy	90	0.44	0.85	0.77	0.53	0.49	0.116	1.09	659	1.09
Lunar	75	1.00	0.44	0.40	0.44	0.40	0.135	0.76	568	1.62
Icy	75	0.73	0.74	0.67	0.54	0.49	0.130	0.98	589	1.16

[a] Surface type.
[b] Aspect angle.
[c] Mass ratio of the binary components.
[d] Axis ratios of the primary.
[e] Axis ratios of the secondary.
[f] Spin (or orbital) frequency of triaxial ellipsoid (or binary).
[g] Binary orbital separation.
[h] Bulk density of the bodies (in kg m^{-3}).
[i] Ratio of χ^2 of model to χ^2 of best-fit model.

Hektor (Fig. 5, *bottom right*), perhaps the most interesting quantity to come out of our simulations, we find $\rho = 2480^{+80}_{-292}$ kg m^{-3}. This value closely confirms an earlier estimate: $\rho \sim 2500$ kg m^{-3} (Weidenschilling 1980).

Figure 6 shows how the best Roche binary model compares to the Dunlap & Gehrels (1969) light-curve data. The differences in light-curve range from one campaign to the next reflect the effect of the observational geometry. Given the simplicity of the model, the agreement is remarkable and lends strong support to the idea that (624) Hektor is a contact binary. The model for Julian day 2,438,795 shows the largest departure from the data. This is to be expected given the small aspect angle, $\theta = 24.8°$. The cross-section

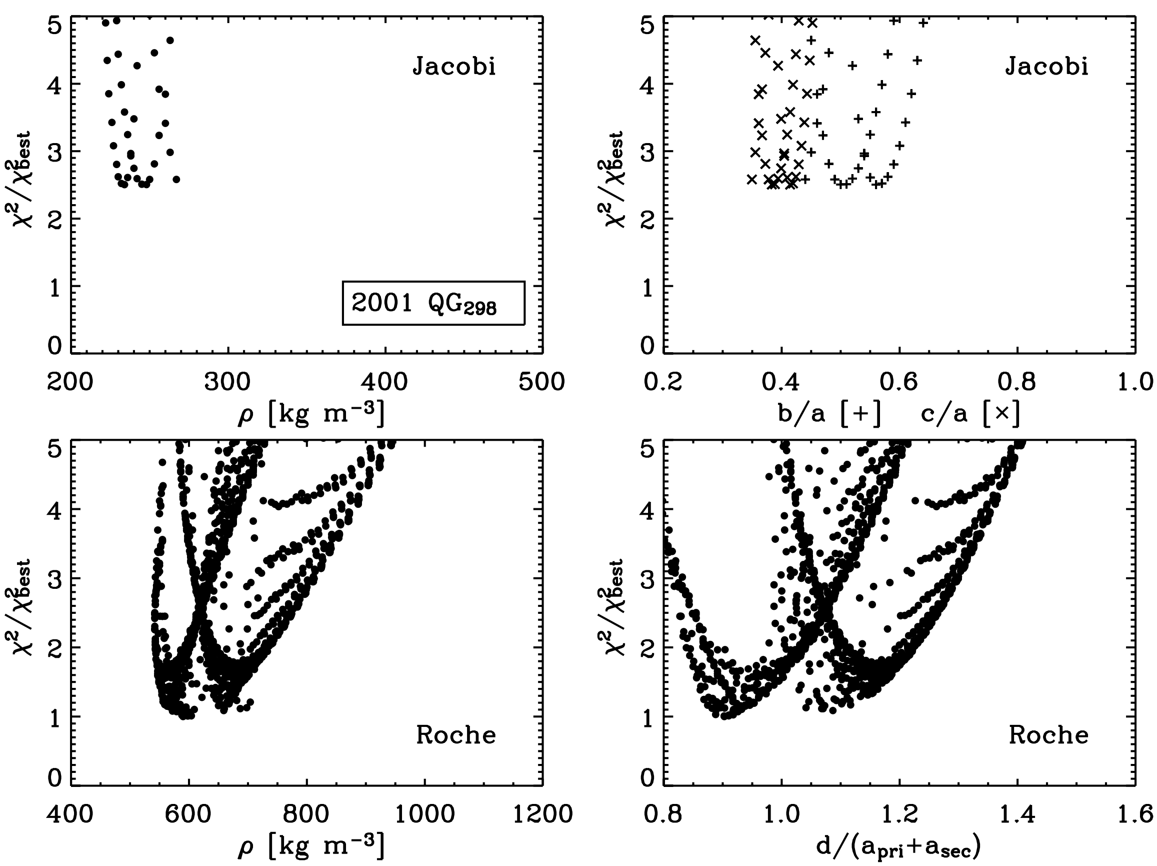

Fig. 8.—Quality of fit vs. bulk density (*top left*) and axis ratios (*top right*) of Jacobi ellipsoid models, and vs. bulk density (*bottom left*) and orbital distance (*bottom right*) of Roche binary models for 2001 QG_{298} light-curve data. Jacobi ellipsoid models are plotted for all four combinations of surface properties and observational geometry listed in Table 5, while Roche binary models are plotted for both lunar- and icy-type surfaces at an aspect angle $\theta = 90°$.

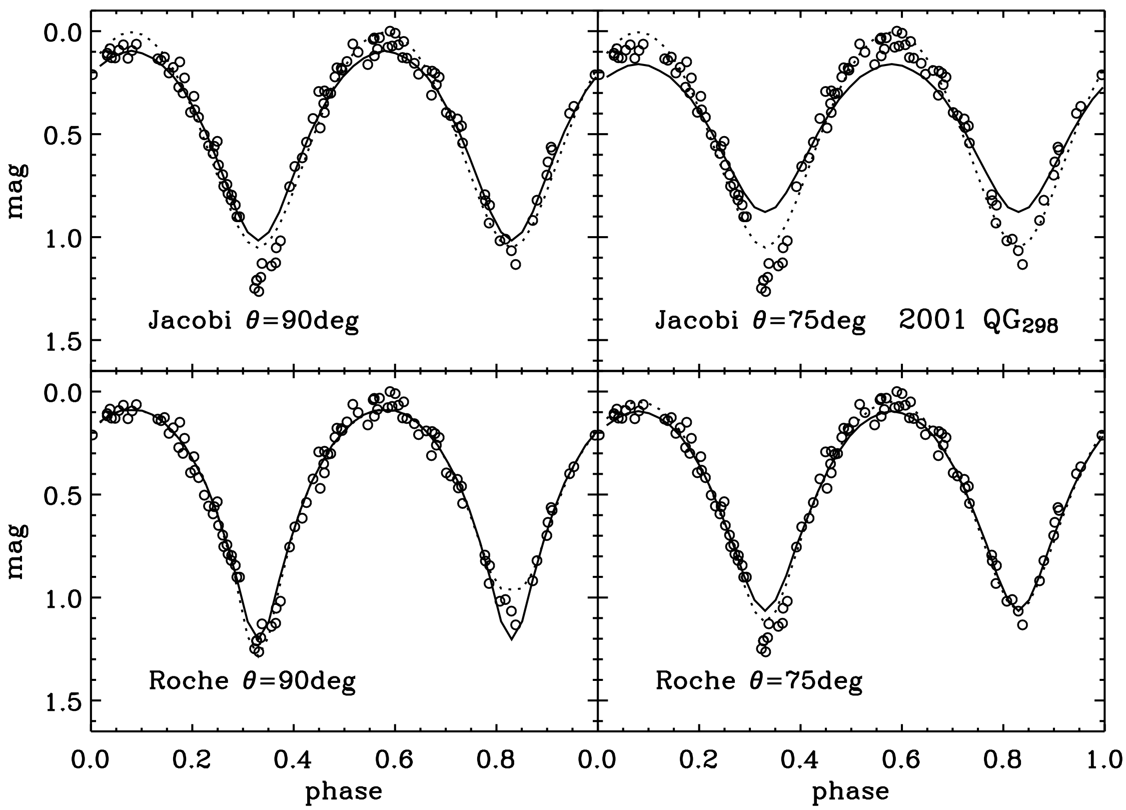

Fig. 9.—Models that best fit the light curve of 2001 QG_{298} for each combination of scattering law and geometry. Solid and dotted lines indicate lunar and icy surface-scattering models, respectively.

of the binary varies little at such unfavorable geometry, and brightness variations must be attributed to irregularities on the surface of the Trojan, which are not accounted for in the model. In Figure 7 we show the best-fit model rendered at the four aspect angles and for eight values of rotational phase. Recent observations using the laser guide star adaptive optics system at the Keck II telescope suggest that (624) Hektor may have a bilobated shape (Marchis et al. 2006b) and lend further support to the results presented here.

3.2. *2001 QG_{298}*

KBO 2001 QG_{298} completes a full rotation every $P = 13.77$ hr, and its brightness varies by $\Delta m = 1.14 \pm 0.04$ mag (Sheppard & Jewitt 2004). The large range of brightness variation and relatively slow rotation provide compelling evidence that 2001 QG_{298} is a contact or very close binary (Sheppard & Jewitt 2004). We attempted to fit both Jacobi ellipsoid and Roche binary models to the light-curve data on 2001 QG_{298}, using the two surface-scattering laws and the two different observational geometries described in §§ 2.3 and 2.4. Table 5 and Figures 8 and 9 present a summary of the best-fit models for different combinations of scattering law and observational geometry.

Clearly, the Roche-binary simulations fit the data better. Furthermore, the binary model favored by the data has a lunar-type surface and an equator-on geometry (see Fig. 9). However, choosing an icy-type surface does not result in a significantly poorer fit. Indeed, Figure 9 (*bottom left*) suggests that an intermediate scattering law is needed to fit the shallower minimum in the light-curve data. Models tilted 15° toward the line of sight are unable to fit the deeper V-shaped minimum in the data. Taking all the Roche simulations into account we find that 2001 QG_{298} should have an orbital separation $d/(A + a) = 0.90^{+0.31}_{-0.14}$ (contact binary) and a bulk density $\rho = 590^{+143}_{-47}$ kg m^{-3}. The uncertainty intervals are established in the same way as was done for (624) Hektor (see § 3.1). Inspection of Table 5 and Figure 8 shows that the best icy-type surface models have $d \sim 1.09$ and $\rho \sim 660$ kg m^{-3}. Given that the chosen surface-scattering laws represent extreme cases (the surface of 2001 QG_{298} probably combines single- and multiple-scattering behavior), we must conclude that the density we find does not depend strongly on the specific surface-scattering properties of the KBO. The same applies to the binary components being in (or very close to) contact. The best-fit Roche binary is rendered in Figure 10. Our results are in good agreement with an independent but similar attempt to fit this object's light curve with a Roche binary model (Takahashi & Ip 2004).

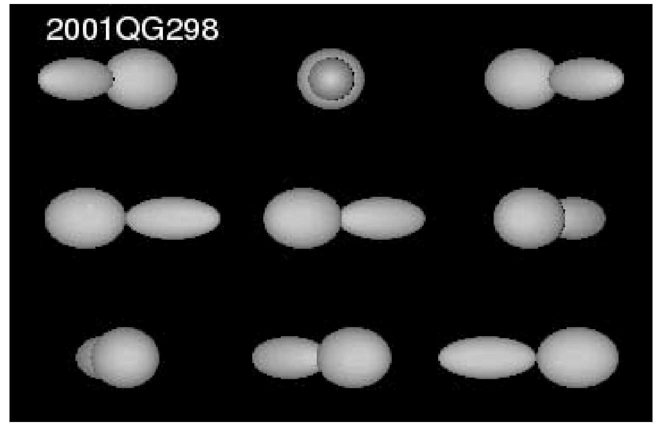

Fig. 10.—Rendering of best-fit Roche binary model for 2001 QG_{298}. Rotational phase ($\phi = 45°, 90°, 135°, 165°, 210°, 240°, 285°, 315°$, and $360°$) runs from left to right and top to bottom.

TABLE 6
2000 GN_{171} Model Fit

ST[a]	θ[b]	q[c]	B/A[d]	C/A[d]	b/a[e]	c/a[e]	$\omega^2/(\pi G\rho)$[f]	$d/(A+a)$[g]	ρ[h]	χ^2/χ^2_{best}[i]
					Jacobi Ellipsoid					
Lunar	90	...	0.62	0.44	...	...	0.342	...	613	1.05
Icy	90	...	0.75	0.50	...	...	0.362	...	579	1.19
Lunar	75	...	0.55	0.41	...	...	0.325	...	645	1.04
Icy	75	...	0.71	0.48	...	...	0.357	...	587	1.20
					Roche Binary					
Lunar	90	0.25	0.92	0.83	0.51	0.48	0.106	1.19	1972	1.09
Icy	90	0.25	0.94	0.87	0.74	0.69	0.084	1.46	2504	1.66
Lunar	75	0.34	0.89	0.81	0.45	0.42	0.108	1.09	1946	1.00
Icy	75	0.25	0.92	0.84	0.61	0.57	0.101	1.28	2067	1.05

[a] Surface type.
[b] Aspect angle.
[c] Mass ratio of the binary components.
[d] Axis ratios of the primary.
[e] Axis ratios of the secondary.
[f] Spin (or orbital) frequency of triaxial ellipsoid (or binary).
[g] Binary orbital separation.
[h] Bulk density of the bodies (in kg m^{-3}).
[i] Ratio of χ^2 of model to χ^2 of best-fit model.

3.3. *2000 GN_{171}*

The rotational properties of KBO 2000 GN_{171} also make it a good candidate contact binary (Sheppard & Jewitt 2004). Its spin period and light-curve range are $P = 8.329$ hr and $\Delta m = 0.61 \pm 0.03$ mag (Sheppard & Jewitt 2002). However, as can be seen in Table 6 and Figures 11 and 12, the light-curve fitting results are not definitive about the nature of this KBO. A Roche binary solution is the one that best fits the data (see Table 6), but it is not significantly better than a single Jacobi ellipsoid model. Inspection of the light-curve fits (Fig. 12) suggests that while the Jacobi ellipsoid model follows better the overall shape of the light curve, it is not able to reproduce the different minima present in the data. A Roche binary solution produces different minima, but

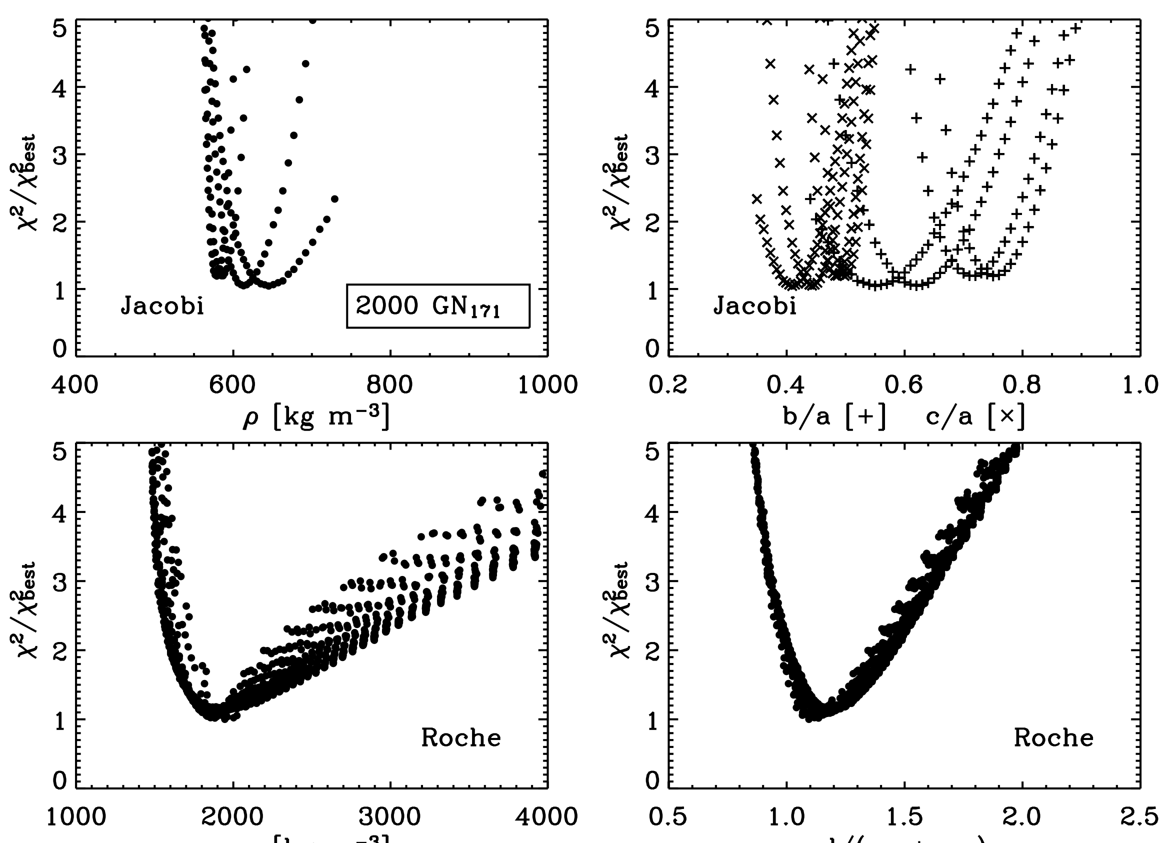

Fig. 11.—Same as Fig. 8 but for 2000 GN_{171} light-curve data. Jacobi ellipsoid models are plotted for all four combinations of surface properties and observational geometry listed in Table 6, while Roche binary models are plotted for a lunar-type surface and aspect angle $\theta = 75°$.

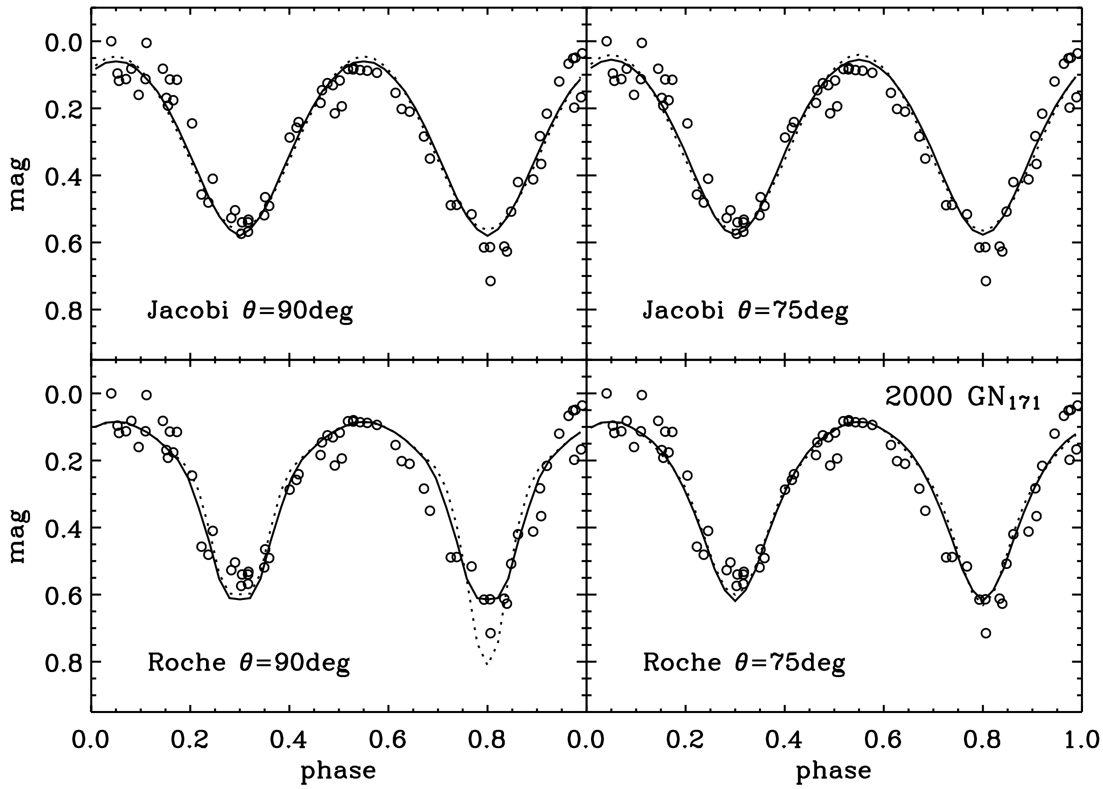

Fig. 12.—Same as Fig. 9 but for 2000 GN_{171}.

seems to require an aspect angle $\theta < 90°$ and a low mass ratio ($q \sim 0.3$) to be able to reproduce a light-curve range as low as $\Delta m = 0.61$ mag. The predicted orbital separation is $d/(A + a) = 1.09^{+0.55}_{-0.10}$. Lunar-type surface models consistently produce better fits than icy-type models, irrespective of the nature (Jacobi ellipsoid or Roche binary) and orientation of 2000 GN_{171}. The inferred density is model dependent, but for each of the two models it does not depend much on scattering properties nor on geometry. If 2000 GN_{171} is taken to be a binary, its density should be $\rho \sim 2000$ kg m^{-3}. If it is an elongated ellipsoid instead it should have a bulk density $\rho \sim 650$ kg m^{-3}. The best Roche binary model for 2000 GN_{171} is rendered in Figure 13.

3.4. *2003 EL$_{61}$*

The light curve of 2003 EL_{61} indicates a rotation period of $P = 3.9$ hr and a light-curve total range of $\Delta m = 0.28 \pm 0.04$

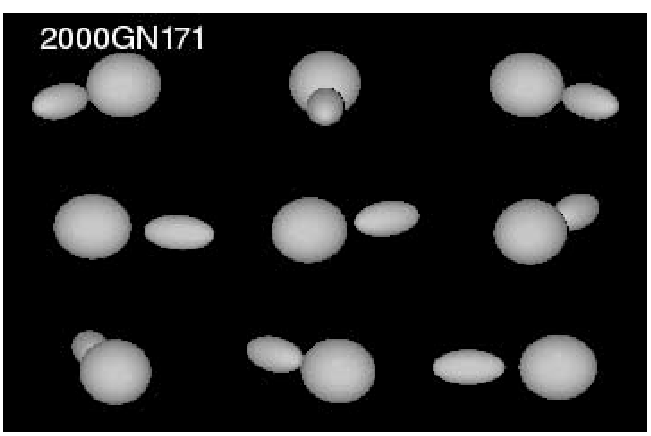

Fig. 13.—Same as Fig. 10 but for 2000 GN_{171}.

(Rabinowitz et al. 2006). The extremely fast rotation of 2003 EL_{61} implies that it must have a high density. Using a hydrostatic equilibrium criterion, Rabinowitz et al. (2006) estimated $\rho \sim 2600$–3340 kg m^{-3}. A binary solution would require a considerably higher (and unrealistic) density than a rotationally deformed ellipsoid. Binarity is also unlikely given the small range of brightness variation: for a binary to produce such a shallow light curve, the pole axis must nearly coincide with the line of sight. Indeed, we find that no Roche binary model is able to satisfactorily fit this object's light-curve data (see Table 7 and Figs. 14 and 15). In the case of Jacobi ellipsoid models, all possible combinations of surface properties or orientation fit the data equally well. This is partly due to the large scatter present in the light-curve data. However, the predicted density ($\rho = 2585^{+81}_{-44}$ kg m^{-3}) depends little on specific choices of surface and geometry and is consistent with the $\rho = 2600$–3340 kg m^{-3} estimate of Rabinowitz et al. (2006). We find that the axis ratios of 2003 EL_{61} should fall in the ranges $b/a = 0.76$–0.88 and $c/a = 0.50$–0.55. The icy scattering law (with $\theta = 75°$; see Table 7) is preferable, as Rabinowitz et al. (2006) found that 2001 EL_{61} has a high albedo (>0.6). The best Jacobi ellipsoid representation of 2001 EL_{61} is shown in Figure 16.

3.5. *(20000) Varuna*

The rotational properties of this object ($P = 6.34$ hr and $\Delta m = 0.42 \pm 0.02$) were interpreted in the context of ellipsoidal figures of equilibrium and a density of $\rho \sim 1000$ kg m^{-3} was derived (Jewitt & Sheppard 2002). Our simulations lend support to this result by showing that (20000) Varuna's light curve is well fit by a Jacobi ellipsoid model. This is apparent from Table 8 and Figures 17 and 18. Figure 16 depicts the Jacobi ellipsoid model of Varuna. As in the case of 2003 EL_{61}, the quality of fit is degenerate as far as surface properties and orientation are concerned. Thus, depending on particular choices of these properties, Varuna's axis ratios lie in the ranges $b/a = 0.63$–0.80 and

TABLE 7
2003 EL_{61} MODEL FIT

ST[a]	θ[b]	q[c]	B/A[d]	C/A[d]	b/a[e]	c/a[e]	$\omega^2/(\pi G\rho)$[f]	$d/(A+a)$[g]	ρ[h]	χ^2/χ^2_{best}[i]
Jacobi Ellipsoid										
Lunar	90	...	0.80	0.52	...	...	0.367	...	2585	1.00
Icy	90	...	0.88	0.55	...	...	0.372	...	2551	1.01
Lunar	75	...	0.76	0.50	...	...	0.363	...	2611	1.02
Icy	75	...	0.86	0.54	...	...	0.371	...	2557	1.00
Roche Binary										
Lunar	90	0.25	0.98	0.94	0.90	0.87	0.039	2.03	24049	6.08
Icy	90	0.25	0.99	0.97	0.96	0.94	0.019	2.65	49286	6.45
Lunar	75	0.25	0.95	0.89	0.79	0.75	0.071	1.58	13339	2.56
Icy	75	0.25	0.97	0.93	0.88	0.85	0.045	1.92	20841	2.46

[a] Surface type.
[b] Aspect angle.
[c] Mass ratio of the binary components.
[d] Axis ratios of the primary.
[e] Axis ratios of the secondary.
[f] Spin (or orbital) frequency of triaxial ellipsoid (or binary).
[g] Binary orbital separation.
[h] Bulk density of the bodies (in kg m^{-3}).
[i] Ratio of χ^2 of model to χ^2 of best-fit model.

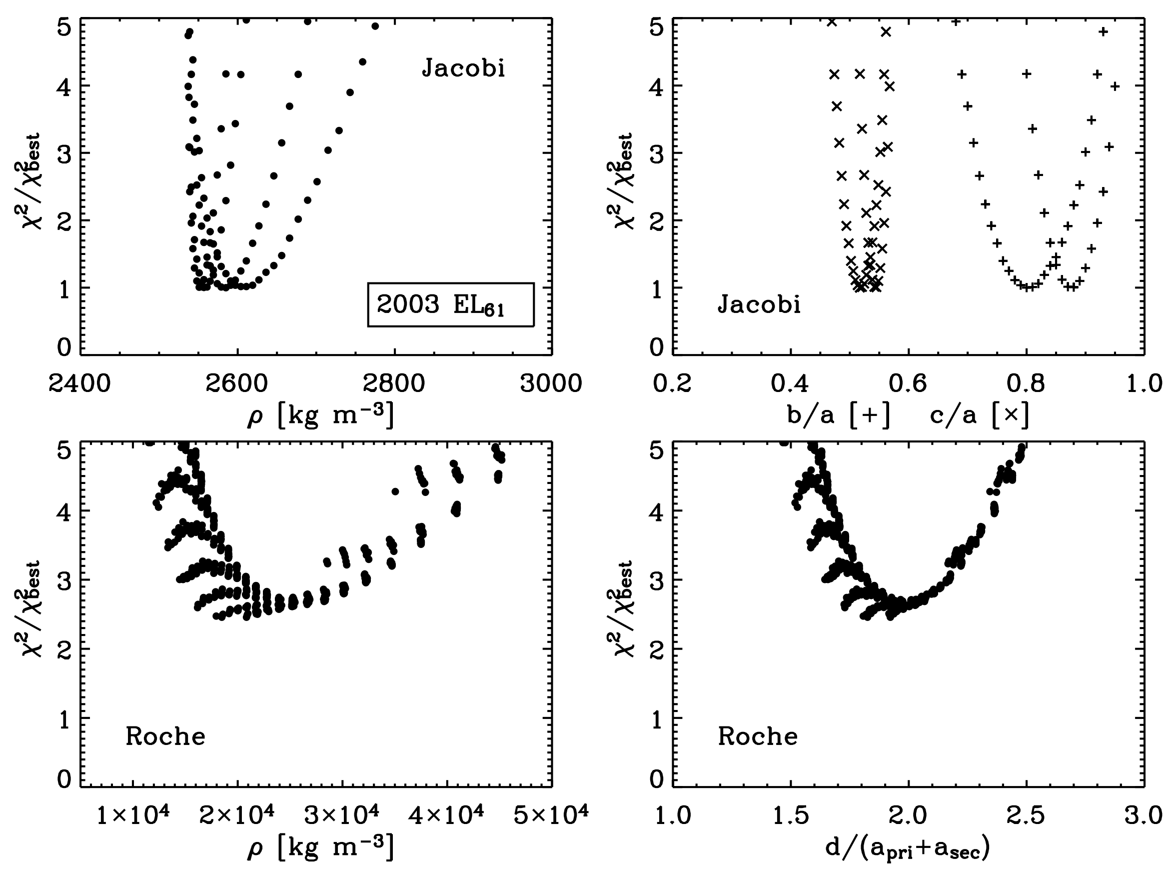

FIG. 14.—Same as Fig. 8 but for 2003 EL_{61} light-curve data. Jacobi ellipsoid models are plotted for all four combinations of surface properties and observational geometry listed in Table 7, while Roche binary models are plotted for an icy-type surface at an aspect angle $\theta = 75°$.

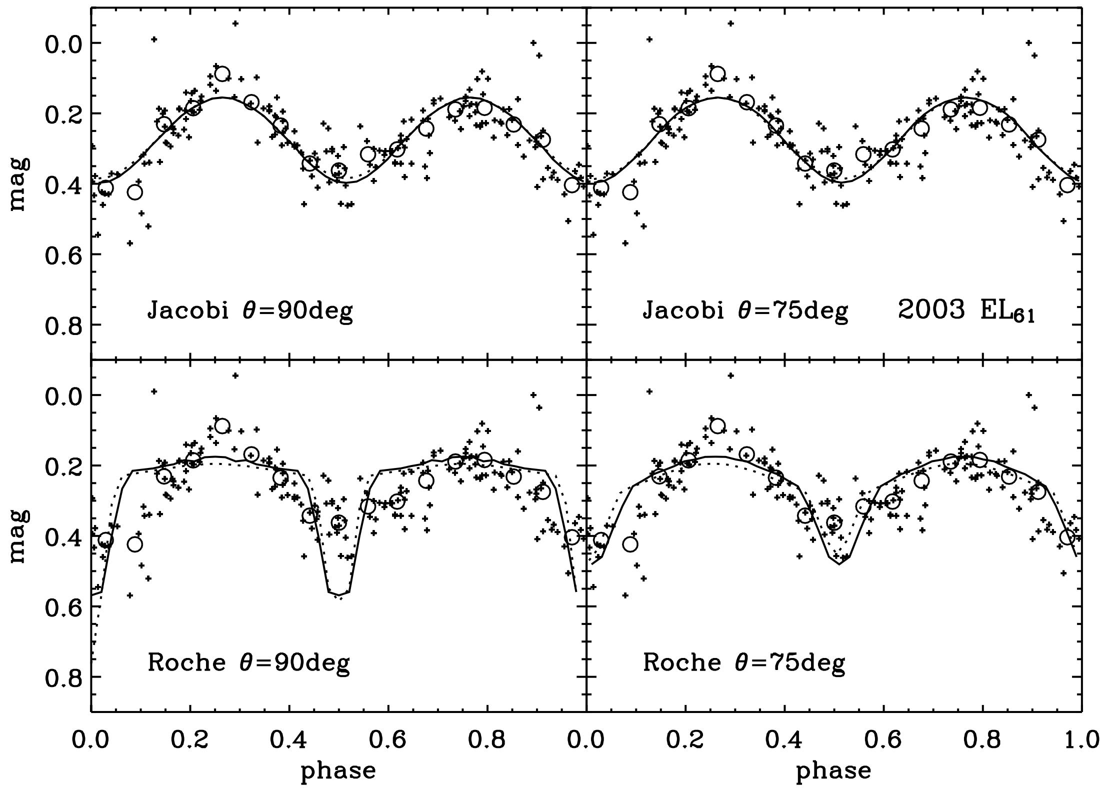

FIG. 15.—Same as Fig. 9 but for 2003 EL_{61}.

$c/a = 0.45$–0.52. The bulk density determination is again much more robust; we find $\rho = 992^{+86}_{-15}$ kg m^{-3}.

4. DISCUSSION

The photometric light curve of 2003 EL_{61} exhibits asymmetries that are not reproduced by the simple Jacobi ellipsoid model. Given the large size of this object ($D_{\rm eq} \sim 1450$; see Table 2), which safely puts it in the gravity regime, we do not expect such irregularities in the light curve to be due to an irregular shape. Instead, if the light-curve features are real, they could have the same origin as Pluto's brightness variation: albedo patches across the object's surface. Like Pluto, 2003 EL_{61} is large enough to hold a thin atmosphere, which might condense on the surface and cause the patches.

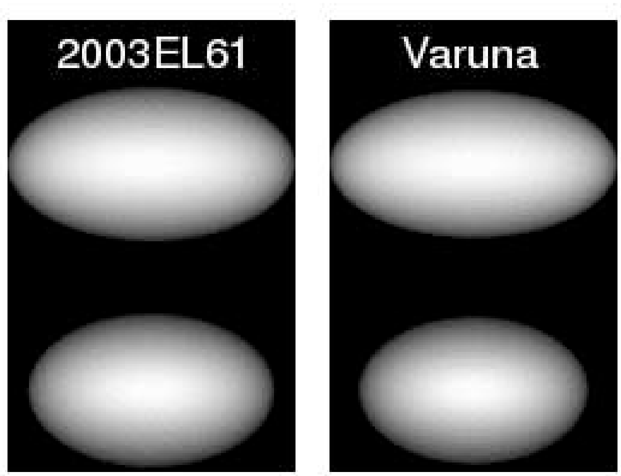

FIG. 16.—Side (*top*) and tip (*bottom*) views of the Jacobi ellipsoid models of 2003 EL_{61} (*left*) and (20000) Varuna (*right*).

The high density derived for (624) Hektor stands in contrast to the low value ($\rho = 800^{+200}_{-100}$ kg m^{-3}) derived for resolved Trojan binary (617) Patroclus (Marchis et al. 2006a). The sizes of these two Trojans are similar; Hektor is 102 ± 2 km in radius while Patroclus is 70 ± 2 km in radius, when measured and interpreted in the same way (Fernández et al. 2003). The low density of Patroclus requires substantial porosity and also suggests an ice-rich composition. Hektor's density is consistent with zero porosity and a smaller or negligible ice fraction. This difference is puzzling, given that the albedos (0.057 ± 0.004 and 0.050 ± 0.005, respectively) are very similar, as are the optical reflectivity gradients ($11.6\% \pm 1\%$ per 1000 Å [Sawyer 1991] and $8.8\% \pm 1\%$ per 1000 Å [Jewitt & Luu 1990], respectively).

Marchis et al. (2006a) argued that the low density and inferred porous, ice-rich composition of (617) Patroclus was an indication that it originated in the outer part of the solar system. The high density of (624) Hektor is hard to explain in this context; does it indicate that (624) Hektor did not form in the outer solar system? Analogously, the similar size and surface properties of these two Jovian Trojans could be used to infer a common origin. A similar density argument was used for the Saturnian irregular satellite Phoebe ($\sim$220 km in radius), but in the opposite direction. The high density of Phoebe ($\rho = 1630 \pm 33$ kg m^{-3}), when compared with that of other (regular) moons of Saturn, has been intepreted as indicative of an outer solar system origin on the basis that it matches the density of Pluto (Johnson & Lunine 2005). As the examples above show, it is difficult to establish a simple relation between formation region and bulk density (there may be no such relation) and therefore the density of a body alone should not be used to infer its origin.

Figure 19 shows the KBO densities from our simulations versus equivalent circular diameter; Pluto and Charon (Person et al.

TABLE 8
(20000) Varuna Model Fit

ST[a]	θ[b]	q[c]	B/A[d]	C/A[d]	b/a[e]	c/a[e]	$\omega^2/(\pi G\rho)$[f]	$d/(A+a)$[g]	ρ[h]	$\chi^2/\chi^2_{\rm best}$[i]
					Jacobi Ellipsoid					
Lunar	90	...	0.69	0.47	...	...	0.354	...	1020	1.16
Icy	90	...	0.80	0.52	...	...	0.367	...	985	1.00
Lunar	75	...	0.64	0.45	...	...	0.346	...	1045	1.17
Icy	75	...	0.77	0.51	...	...	0.364	...	992	1.00
					Roche Binary					
Lunar	90	0.25	0.92	0.84	0.61	0.57	0.101	1.28	3563	5.48
Icy	90	0.25	0.95	0.88	0.76	0.72	0.078	1.52	4657	8.12
Lunar	75	0.25	0.92	0.83	0.51	0.48	0.106	1.19	3399	2.95
Icy	75	0.25	0.93	0.85	0.66	0.62	0.096	1.34	3780	3.53

[a] Surface type.
[b] Aspect angle.
[c] Mass ratio of the binary components.
[d] Axis ratios of the primary.
[e] Axis ratios of the secondary.
[f] Spin (or orbital) frequency of triaxial ellipsoid (or binary).
[g] Binary orbital separation.
[h] Bulk density of the bodies (in kg m^{-3}).
[i] Ratio of χ^2 of model to χ^2 of best-fit model.

2006) are plotted for comparison. The sizes of 2001 QG_{298} and 2001 GN_{171} were calculated from their absolute magnitude assuming a 0.04 albedo, and the error bars extend the albedo to 0.10. The size of (20000) Varuna is from Jewitt et al. (2001) and that of 2003 EL_{61} is calculated using its mass (Rabinowitz et al. 2006) and the density derived here (see also Table 2). A trend of increasing density with size is clear. Such relation may be caused by (1) a difference in composition (ice/rock ratio), with bigger objects having larger rock fractions, or (2) a trend in porosity, with larger objects being more compacted than their smaller counterparts, likely due to larger internal pressure. Although the latter effect is certainly present, it is unclear if it is the dominant

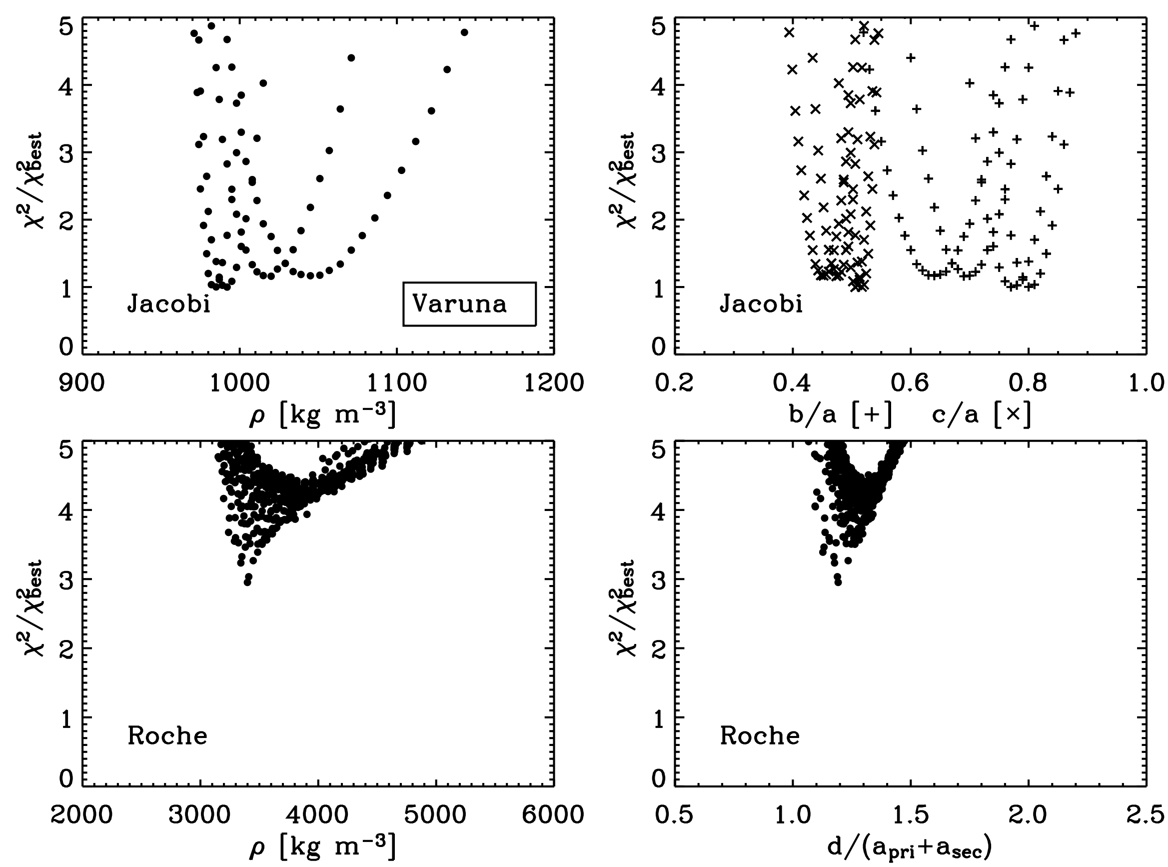

Fig. 17.—Same as Fig. 8 but for (20000) Varuna light-curve data. Jacobi ellipsoid models are plotted for all four combinations of surface properties and observational geometry listed in Table 8, while Roche binary models are plotted for a lunar-type surface and an aspect angle $\theta = 75°$.

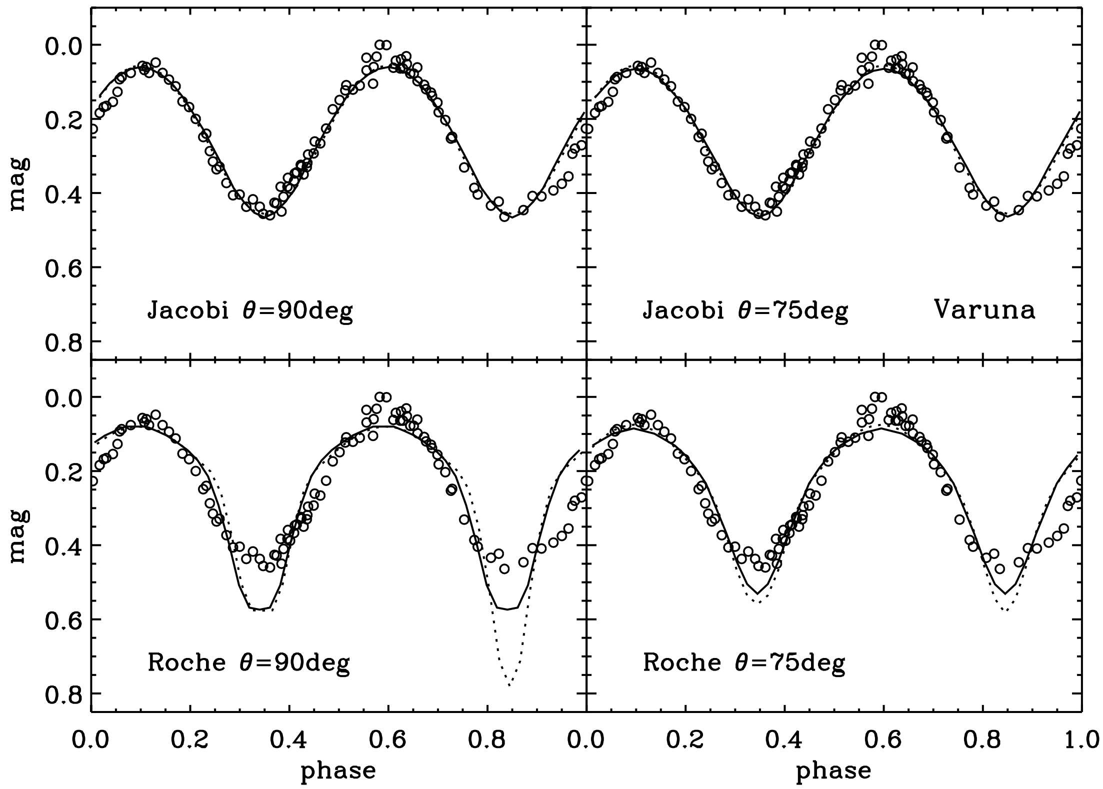

FIG. 18.—Same as Fig. 9 but for (20000) Varuna.

cause for the trend. This size-density relation has been noted before (Jewitt 2002) and seems to be present in different populations, e.g., KBOs and planetary satellites (Jewitt 2007).

5. THE FRACTION OF CONTACT BINARIES IN THE KUIPER BELT

Our simulations can be used to determine the light curve range of Roche binaries at arbitrary observing geometries and for two different surface types. We make use of this feature to refine an earlier estimate of the contact binary fraction in the Kuiper Belt (KB; see Sheppard & Jewitt 2004). Leone et al. (1984) argued that light curves with ranges between 0.9 and 1.2 mag must

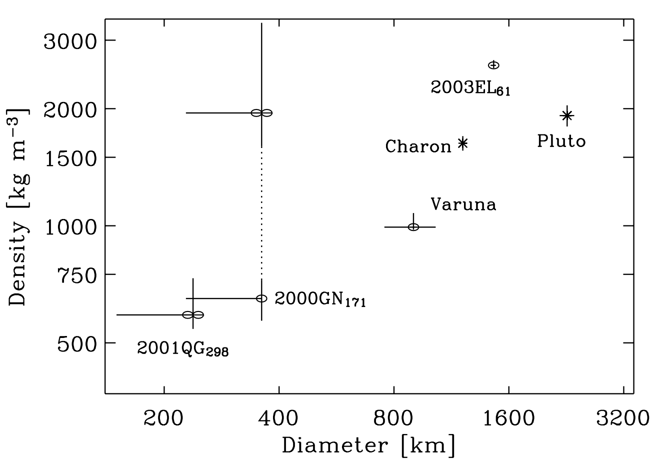

FIG. 19.—Log density vs. log equivalent circular diameter for the four KBOs modeled. Jacobi ellipsoid fits are indicated by single ellipsoid symbols, and Roche binary fits are indicated by double ellipsoid symbols. Pluto and Charon are plotted for comparison. KBO 2000 GN_{171} is plotted twice (*dotted line*).

be produced by tidally deformed contact binaries (see also Weidenschilling 1980). While the maximum range of 1.2 mag is valid for lunar-type surfaces having negligible limb darkening, our simulations show that Roche binaries with icy-type surfaces (and thus significant limb darkening) can produce light-curve ranges up to 1.57 mag. We searched our models for the binaries that produce these maximal light-curve ranges (1.2 mag for lunar surface and 1.57 mag for icy surface) when observed equator-on, i.e., at aspect angle $\theta = 90^\circ$. The aspect angle is measured between the line of sight and the pole axis of the binary. As the pole axis of such a binary moves away from the equator-on configuration (as the aspect angle approaches 0°) the light-curve range becomes smaller and smaller; let us denote by $\theta_{\rm min}$ the aspect angle at which the light-curve range reaches 0.9 mag. If we assume that the pole axes of KB contact binaries are randomly oriented in space, then the detected contact-binary fraction is less than the true fraction by a (geometrical correction) factor $\cos\theta_{\rm min}$.

Using our simulations we find the geometrical correction factor to be $\sim\cos(81.4^\circ) = 0.15$ for lunar-type surfaces and $\sim\cos(70.7^\circ) = 0.33$ for binaries with an icy-type surface (see Fig. 20). We use the fraction of 1/34 objects with large (>0.9 mag) light-curve range measured by Sheppard & Jewitt (2004) as it constitutes the largest homogeneous survey for variability. Therefore, considering only lunar-type surfaces the true fraction of contact binaries is $f \sim 1/(34 \times 0.15) \sim 0.20$. If we consider icy-type surfaces then we estimate the fraction to be $f \sim 1/(34 \times 0.33) \sim 0.09$. Two arguments make the latter of the two estimates a strong lower limit for the true fraction of contact (or close) KB binaries. First, the two surface types used here are simplified limiting models of how real planetary surfaces scatter light. Real objects presumably exhibit a degree of limb darkening between the two simulated here. Secondly, contact binaries with relatively low mass ratios produce shallower light curves, which fall below the 0.9 mag threshold adopted here and are not accounted for. Our

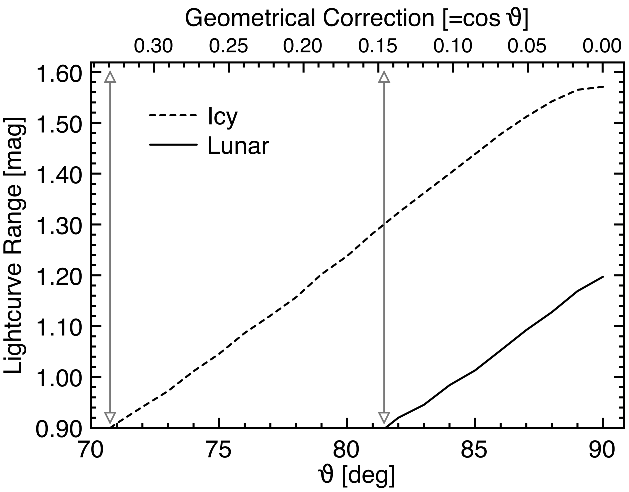

FIG. 20.—Light-curve range as function of aspect angle θ for maximal Δm Roche binaries with both lunar- and icy-type surfaces. Top x-axis shows probability that the binary is observed at equal or larger θ. See text for details.

estimate, new in that it includes the effect of surface scattering, substantiates the idea that a considerable population of contact/close binary objects in the KB may await discovery (Sheppard & Jewitt 2004).

The Pan-STARRS all-sky survey[3] will scan the entire visible sky, down to $m_R \sim 24$, on a weekly basis (Kaiser et al. 2005). Besides detecting all moving objects to that brightness limit, this cadence will allow (sparsely sampled) time-series photometric studies, and thus the detection of high-variability candidates, suitable for follow-up observations. The survey will therefore significantly improve the estimate of the contact binary fraction. The intrinsic fraction of KB contact binaries can provide important constraints on binary formation mechanisms (e.g., Goldreich et al. 2002) and collisional evolution in the KB region (Petit & Mousis 2004).

[3] See http://pan-starrs.ifa.hawaii.edu/.

6. SUMMARY

Mathematically unique interpretations of rotational light-curve data are generally impossible. Nevertheless, light curves can, under physically plausible assumptions, convey invaluable information about the spins, shapes, and densities of small solar system bodies. In this work we have explored the role of surface-scattering properties on the derivation of bulk densities from rotational light curves using a quantitative model of rotationally deformed bodies. We find that:

1. With few exceptions, the choice of a particular scattering function does not strongly affect the densities we obtain from our simulations. Instead, the presence of surface irregularities (lumps) and some albedo variegation (spots) on the objects sets the limit to the precision of our density estimates; surface lumps and spots make it impossible to find one idealized equilibrium shape that matches the light curve, leading to some degeneracy in the fits.
2. Our density estimates suggest a trend of increasing density with size. It is still unclear if such a relation is mainly due to composition, to a trend in porosity, or to a combination of both.

Confirming previous inferences, we find that:

3. The light curves of (20000) Varuna and 2003 EL_{61} are well matched by rotational equilibrium models in which the bodies are deformed by rotation into a triaxial shape. Jacobi ellipsoid models with uniform surface albedo and a range of limb-darkening functions have been used to derive the bulk densities (Varuna, 992^{+86}_{-15} kg m^{-3}; 2003 EL_{61}, 2551^{+115}_{-10} kg m^{-3}).
4. The light curves of Jovian Trojan (624) Hektor and KBO 2001 QG_{298} are well described by contact-binary models in which the densities are 2480^{+292}_{-80} and 590^{+143}_{-47} kg m^{-3}, respectively.
5. The high incidence of KBO light curves consistent with a contact binary interpretation suggests that these bodies are common in the Kuiper Belt.

P. L. is grateful to the Fundação para a Ciência e a Tecnologia (BPD/SPFH/18828/2004) for financial support. This work was supported, in part, by a grant from the NSF to D. C. J.

REFERENCES

Belskaya, I. N., Ortiz, J. L., Rousselot, P., Ivanova, V., Borisov, G., Shevchenko, V. G., & Peixinho, N. 2006, Icarus, 184, 277
Cellino, A., Zappala, V., & Farinella, P. 1989, Icarus, 78, 298
Chandrasekhar, S. 1963, ApJ, 138, 1182
———. 1969, Ellipsoidal Figures of Equilibrium (New Haven: Yale Univ. Press)
Chandrasekhar, S., & Lebovitz, N. R. 1962, ApJ, 136, 1037
Cruikshank, D. P. 1977, Icarus, 30, 224
———. 2005, Adv. Space Res., 36, 1070
de Angelis, G. 1995, Planet. Space Sci., 43, 649
Degewij, J., Tedesco, E. F., & Zellner, B. 1979, Icarus, 40, 364
Dunlap, J. L., & Gehrels, T. 1969, AJ, 74, 796
Fernández, Y. R., Sheppard, S. S., & Jewitt, D. C. 2003, AJ, 126, 1563
Goldreich, P., Lithwick, Y., & Sari, R. 2002, Nature, 420, 643
Hartmann, W. K., & Cruikshank, D. P. 1978, Icarus, 36, 353
———. 1980, Science, 207, 976
Hicks, M. D., Simonelli, D. P., & Buratti, B. J. 2005, Icarus, 176, 492
Jeans, J. H. 1919, Problems of Cosmogony and Stellar Dynamics (Cambridge: Cambridge Univ. Press)
Jewitt, D. 2002, in Proc. Asteroids, Comets, Meteors–ACM 2002, ed. B. Warmbein (ESA SP-500; Noordwijk: ESA), 11
———. 2007, in Trans-Neptunian Objects and Comets, ed. D. Jewitt, A. Morbidelli, & H. Rauer (Berlin: Springer), in press
Jewitt, D., Aussel, H., & Evans, A. 2001, Nature, 411, 446
Jewitt, D. C., & Luu, J. X. 1990, AJ, 100, 933
Jewitt, D. C., & Sheppard, S. S. 2002, AJ, 123, 2110
Johnson, T. V., & Lunine, J. I. 2005, Nature, 435, 69
Kaasalainen, M., Mottola, S., & Fulchignoni, M. 2002, in Asteroids III, ed. W. F. Bottke, Jr., et al. (Tucson: Univ. Arizona Press), 139
Kaasalainen, M., & Torppa, J. 2001, Icarus, 153, 24
Kaasalainen, M., Torppa, J., & Muinonen, K. 2001, Icarus, 153, 37
Kaiser, N., et al. 2005, BAAS, 37, 1409
Leone, G., Paolicchi, P., Farinella, P., & Zappala, V. 1984, A&A, 140, 265
Li, J.-Y. 2005, Ph.D. thesis, Univ. Maryland, College Park
Marchis, F., et al. 2006a, Nature, 439, 565
———. 2006b, IAU Circ., 8732, 1
Millis, R. L. 1977, Icarus, 31, 81
Person, M. J., Elliot, J. L., Gulbis, A. A. S., Pasachoff, J. M., Babcock, B. A., Souza, S. P., & Gangestad, J. W. 2006, AJ, 132, 1575
Petit, J.-M., & Mousis, O. 2004, Icarus, 168, 409
Rabinowitz, D. L., Barkume, K., Brown, M. E., Roe, H., Schwartz, M., Tourtellotte, S., & Trujillo, C. 2006, ApJ, 639, 1238
Russell, H. N. 1906, ApJ, 24, 1
Sawyer, S. R. 1991, Ph.D. thesis, Univ. Texas, Austin
Sheppard, S. S., & Jewitt, D. C. 2002, AJ, 124, 1757
———. 2004, AJ, 127, 3023
Takahashi, S., & Ip, W.-H. 2004, PASJ, 56, 1099
Weidenschilling, S. J. 1980, Icarus, 44, 807
Wijesinghe, M. P., & Tedesco, E. F. 1979, Icarus, 40, 383